

## Research Article

# Dynamic Structural Assessment of Blast Wall Designs on Military-Based Vehicle Using Explicit Finite Element Approach

Muhammad Arif Husni Mubarak,<sup>1</sup> Aditya Rio Prabowo ,<sup>1</sup> Teguh Muttaqie ,<sup>2</sup>  
and Nurul Muhayat <sup>1</sup>

<sup>1</sup>Department of Mechanical Engineering, Universitas Sebelas Maret, Surakarta, Indonesia

<sup>2</sup>Research Center for Hydrodynamics Technology, National Research and Innovation Agency (BRIN), Surabaya, Indonesia

Correspondence should be addressed to Aditya Rio Prabowo; [aditya@ft.uns.ac.id](mailto:aditya@ft.uns.ac.id)

Received 30 June 2022; Revised 24 August 2022; Accepted 25 August 2022; Published 13 September 2022

Academic Editor: Mijia Yang

Copyright © 2022 Muhammad Arif Husni Mubarak et al. This is an open access article distributed under the Creative Commons Attribution License, which permits unrestricted use, distribution, and reproduction in any medium, provided the original work is properly cited.

Explosion load studies are an essential part of shield engineering design. This is especially true for explosion-proof plates, which are used in order to reduce the impact of explosions, which have the potential to cause substantial damage to structural elements. The purpose of this study is to detail the explosion phenomenon and the response of sandwich panel structures under explosive loading. The finite element method (FEM) is used to model the dynamic structural response to explosions. Explicit finite element modeling and analysis are performed using ABAQUS CAE software. An air explosion simulation code is used to determine the blast load on the lower skin plate of a test panel on a typical armored personnel vehicle. Structural analysis is carried out with respect to displacement, von-Mises stress, and internal kinetic energy. Three variations of explosive loads are considered in the simulation in order to better compare the responses of the structures. Three different design variants and materials are considered, including honeycomb, stiffener, and corrugated geometric models and mild steel, medium carbon steel, and alloy steel materials. The results provided by this study pave the way toward the development of guidelines for the design of lightweight structural reinforcement elements.

## 1. Introduction

A blast load is a load applied to a structure or object from a blast wave, which is described by a combination of overpressure and impulse or duration. In cases of uncontrolled unloading, such as IEDs, explosive loading is generated from explosives with a payload weight (kg) and type determined directly by the explosive device. During the detonation of high explosives [1], a blast wave is generated, impacting the structure through the application of incident overpressure (P<sub>so</sub>) [2] which, in turn, is reflected back from the structure in the form of reflected excess pressure (PCa) [3, 4].

Research on the response of the geometric structure of a plate to impact and various active loads [5–13], including air blast loading, has been carried out over the past few decades. Explosive loading due to landmines and improvised explosive devices (IEDs) poses a significant threat to military

vehicles and civilian infrastructure. According to the Landmine Monitor report, the number of victims from the use of landmines and improvised explosive devices (IEDs) in 2020 increased by 20%, compared to the previous 12 months as a result of the “increased armed conflict and contamination” of land with improvised mines. More than 7000 people were killed or injured in 54 countries and territories [14]. This highlights the need for better mine-resistant vehicles, especially for peacekeepers. Efforts have been made to improve the response of civil structures and transport vehicles to blast loads in order to address the risks involved. It is essential to understand the loads caused by the explosion and the damage to the structure. With proper engineering and the selection of materials with higher strength and hardness (which is useful in ballistic applications), the ability of the designed structure to respond to explosions will increase [15, 16]. Thus, the investigation of the use of layered

structures as a means to withstand blast loads resulting from explosions has become more significant.

Several types of studies on air blasts using both software and experimental simulations have been carried out, as there are limitations to each method. Experimental, numerical, and analytical methods have been utilized to study the impact of air blasts. In order to understand the safety of structures under blast waves, it is essential to describe and define some basic and relevant concepts. The concept of an explosion describes a rapid phenomenon of physical, chemical, or nuclear conservation, in which the transformation of potential energy into mechanical and thermal work cannot be separated. This work is carried out by expanded gas, which is compressed during the phenomenon [17]. Sandwich structures can dissipate considerable amounts of energy and can generate large plastic deformation under impact/explosion loads; therefore, they have been widely used in various fields, including aerospace, marine, and railway engineering. Xue and Hutchinson compared the performance of metal sandwich panels under pulsed blast loads with solid panels made of the same material and weight. The results demonstrated that the sandwich panels outperformed the solid panels, especially concerning water spray [18]. Dharmasena et al. conducted explosion tests to study the dynamic response of square honeycomb core sandwich and solid panels. The results indicated that the honeycomb sandwich panels produced less deflection than solid panels of the same mass [19]. Zhu and Khanna conducted air-jet experiments to study the dynamic response of honeycomb sandwich panels. The results showed that the thickness of the panel and the core density significantly affect the deformation/failure mode [20].

Several studies have shown that the structural configuration of sandwich panels still needs to be optimized, in terms of their function in resisting air blasts. Markose and Rao have proposed an APV hull plate optimization method using a single panel and mild steel materials to resist the effects of air blast loads [21]. Plate geometries limited to single flat plates, commonly used materials, and explosion loads limited to small loads are critical for technological advancement, especially that of armored vehicles. Our focus and key contribution in this study are that we use the more complex geometric variations (honeycomb, stiffeners, and corrugations), materials with better properties (mild steel, medium carbon steel, and alloy steel), and higher blast loads (21 kg, 28 kg, and 35 kg) for comparison. We use the CONWEP system in the ABAQUS CAE software to investigate the dynamic response of sandwich panels under blast load. The interaction between the blast wave and the plate, as well as the displacement mode, stress mode, and internal energy, is considered in the experiment. Numerical simulations are also carried out, in order to study the sandwich panel response process.

## 2. Literature Review

**2.1. Air Blast Loading.** A blast wave consists of a high-intensity pressure front, propagating outward from the center of the explosive into the surrounding air. As the shock wave expands, its amplitude decreases, its duration increases, and

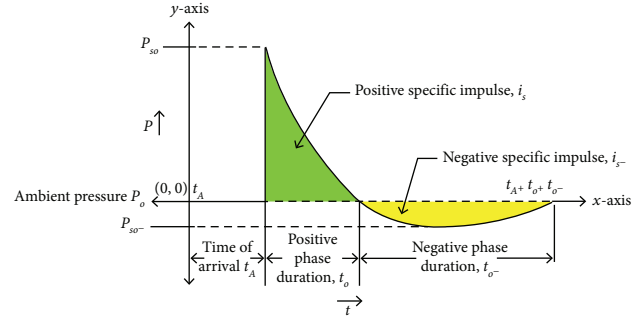


FIGURE 1: Free air blast pressure time history.

its detonation velocity decreases [22, 23]. Figure 1 shows a typical pressure curve for an explosion in free air. The shock wave is characterized by two phases: an overpressure phase and a low-pressure phase. The positive phase is characterized by a sudden linear increase in pressure at the peak of the pressure front, followed by an exponential drop back to standard atmospheric pressure ( $P_0$ ), which is then followed by a suction phase, in which the air is absorbed and a partial vacuum is formed [22].

It can be seen, from Figure 1, that the maximum negative overpressure ( $P_{S^-}$ ) is much smaller than the maximum positive overpressure ( $P_{OP}$ ), and its limit is 1 atm ( $\approx 0.1$  MPa). However, the duration of the negative phase is 2 to 3 times longer than that of the positive phase [24]. Generally, blast design standards and manuals include the IS 6922 Bureau of Indian Standards (BIS) and TM 5-855-1. The U.S. Department of Defense recommends using only the positive pressure phase of blast loads in structural analysis and design, assuming that the negative pressure phase is generally much weaker, and does not significantly affect the structural response/damage [25, 26].

The time history of the blast wave pressure can be formulated using the modified Friedlander equation:

$$p(t) = (p_{so} - p_o) \left[ 1 - \frac{t - t_A}{t_o} \right] e^{-(t - t_A)/\theta}, \quad (1)$$

where  $p_o$  is the ambient pressure,  $t$  is the overall duration,  $t_A$  is the arrival time,  $t_o$  is the positive phase duration, and  $\theta$  is the time decay constant [27]. The peak pressure of the blast wave ( $P$ ) can be written using the following equation:

$$P = K \left[ \frac{m}{r^3} \right], \quad (2)$$

where  $K$  is an explosive material parameter,  $m$  is the explosive mass, and  $r$  is the stand-off distance [28]. The imparted impulse ( $I$ ) is obtained by integrating the pressure acting with respect to the time duration of the loading:

$$I = \int_{t_A}^{t_A + t_o} p dt, \quad (3)$$

where  $p$  represents the applied pressure due to the blast loading function in CONWEP and  $t_o$  is the duration of loading.

**2.2. FEM Explicit Dynamic Simulation.** In ABAQUS/Explicit models, the explicit integration uses center interpolation (i.e., H). At time  $t$ , when the dynamic equilibrium condition is satisfied, the nodal force (external force  $P$  minus internal force  $I$ ) can be calculated by multiplying the mass matrix  $M$  by the acceleration matrix:

$$Mu = P - I. \quad (4)$$

When increasing from the initial time  $t$ , the acceleration can be calculated as follows:

$$u|_t = (M)^{-1}(P - I)|_t. \quad (5)$$

As the lumped mass matrix is always used in the explicit integration algorithm, the acceleration can be obtained directly without solving the equations. The acceleration of a given node can be determined using only the nodal mass and nodal force, which can significantly reduce the computation time. Assuming that the acceleration remains constant for a particular time increment, the increase in velocity can be calculated using central interpolation. The velocity at the midpoint of the current time increment is obtained by adding the velocity increment to the velocity at the midpoint of the previous time increment:

$$\dot{u}|_{\left(t+\frac{1}{2}\Delta t\right)} = \dot{u}|_{\left(t+\frac{1}{2}\Delta t\right)} + \frac{1}{2} \cdot \left( \Delta t|_{\left(t+\frac{1}{2}\Delta t\right)} + \Delta t|_t \right) \cdot u|_t. \quad (6)$$

The deformation at the end of the time increment can be calculated by integrating the velocity:

$$u|_{(t+\Delta t)} = u|_t + \Delta t \cdot u|_{\left(t+\frac{1}{2}\Delta t\right)}. \quad (7)$$

The stability of the explicit procedure is conditional; that is, the time increment cannot exceed the  $t_{\text{stable}}$  constraint, which can be estimated by the following equation:

$$\Delta t_{\text{stable}} = \frac{2}{\omega_{\text{max}}} \left( \sqrt{1 + \xi^2} - \xi \right). \quad (8)$$

Modeling using explicit time integration is limited by the Courant–Friedrichs–Levy condition [29]. This condition implies that the time step is limited, so a disturbance (e.g., stress wave) cannot travel further than the smallest characteristic element dimension in the mesh in a single time

step. Thus, the time step criterion for solution stability is calculated as follows:

$$dt_{\text{cou}} < \min\left(\frac{dx}{c}, \frac{dy}{c}\right), \quad (9)$$

where  $dt$  is the time increment,  $dx$  and  $dy$  are the characteristic dimensions of an element, and  $c$  is the local speed of sound in an element. Based on this condition, one can conclude that a smaller mesh size implies smaller time steps and, consequently, longer calculation time.

**2.3. CONWEP (Conventional Weapons Effects Program).** An appropriate choice for numerical simulation analysis of the fluid-structure interaction problem under air blast loading is to utilize CONWEP's built-in explosion generation function. CONWEP uses an empirical equation to calculate the shock wave pressure acting on a surface [21]. In the CONWEP approach, the explosion will produce a pressure wave, as shown in Figure 1.

The structural interactions are described numerically using the CONWEP (conventional weapons effects program) payload property available in the ABAQUS software, considering the mass of TNT to describe the explosive charge [30]. The CONWEP algorithm, developed by Kingery and Bulmash, calculates the angle of incidence by combining the value of the reflected pressure (normal incident) and the value of the incident pressure (side on incidence). The following equation can be used to calculate the pressure:

$$Z = \frac{R}{W^{1/3}}, \quad (10)$$

where  $R$  is the stand-off distance, which refers to the distance from the center of the explosion to the target structure, and the greater the stand-off distance, the less structural damage from the blast wave can be expected.  $R$  can be easily expressed as follows:

$$R = \sqrt{h^2 + x^2}. \quad (11)$$

Furthermore,  $W$  is the weight of the explosive charge. The total air blast overpressure ( $P_{\text{total}}$ ) can be determined by combining the angle of incidence ( $\theta$ ), depending on the incident overpressure ( $P_{\text{io}}$ ) and reflected overpressure ( $P_{\text{ro}}$ ) [31], as follows:

$$P_{\text{total}}(t) = \begin{cases} [P_{\text{ro}}(t) - 2P_{\text{io}}(t)]\cos\theta^2 + [\cos\theta + 1]P_{\text{io}}(t), & \cos\theta \geq 0, \\ P_{\text{io}}(t), & \cos\theta < 0, \end{cases} \quad (12)$$

$$P_{\text{io}}(t) = (P_{\text{so}} - P_{\text{o}}) \left( 1 - \frac{t - t_a}{t_o} \right) e^{-(\beta t - t_a/t_o)},$$

$$P_{\text{ro}}(t) = 2P_{\text{io}}(t) + \frac{(\gamma + 1)\{P_{\text{io}}(t)\}^2}{2\gamma P_a + (\gamma - 1)P(t)}$$

where  $P_{so}$  represents the peak incident pressure (subscripts have been used to denote the peak incident pressure and side pressure [32]),  $P_o$  represents the ambient pressure,  $t_a$  indicates the arrival time of the shock wave propagating to the target structure,  $t_o$  is the time duration of the positive phase,  $\beta$  is a dimensionless decay coefficient that depends on the shape of the shock wavefront [33], and  $\gamma$  is the ratio of the specific heat of air.

**2.4. Johnson–Cook Model.** In cases such as those considered here, TNT is usually modeled using the Johnson–Cook model. An elastoplastic material model was used with Johnson–Cook strain hardening and damage initiation. This model has been widely used in engineering, due to its simple form and few parameters [34]. The Johnson–Cook strain rate dependence assumes

$$\bar{\sigma} = \sigma^0(\bar{\epsilon}_{eq}^p, T)R(\bar{\epsilon}_{eq}^p). \quad (13)$$

$$\bar{\epsilon}_{eq}^p = \dot{\epsilon}_0 \exp\left[\frac{1}{C}(R-1)\right] \text{ for } \bar{\sigma} \geq \sigma^0, \quad (14)$$

where  $\bar{\sigma}$  is the yield stress at nonzero strain rate,  $\bar{\epsilon}_{eq}^p$  is equivalent plastic strain rate,  $\dot{\epsilon}_0$  is the reference strain rate,  $\sigma^0(\bar{\epsilon}_{eq}^p, T)$  is the static yield stress, and  $R(\bar{\epsilon}_{eq}^p)$  is the ratio of the yield stress at nonzero strain rate to the static yield stress.

The equivalent von-Mises yield stress can, therefore, be expressed as follows:

$$\bar{\sigma} = \left(A + B(\bar{\epsilon}_{eq}^p)^n\right) \left(1 + C \ln\left(\frac{\bar{\epsilon}_{eq}^p}{\dot{\epsilon}_0}\right)\right) (1 - (T^*)^m), \quad (15)$$

where  $A$ ,  $B$ ,  $n$ ,  $C$ , and  $m$  are material parameters, and  $T$  is expressed as follows:

$$T^* = \begin{cases} 0, & \text{for } T < T_r, \\ \frac{T - T_r}{T_m - T_r} & \text{for } T_r \leq T \leq T_m \\ 1, & \text{for } T > T_m, \end{cases} \quad (16)$$

where  $T$  is the material temperature (K),  $T_m$  is the melting temperature of the material, and  $T_r$  is the room temperature.

The damage initiation and evolution can also be modeled by the Johnson–Cook approach [35]. The damage is based on the value assumed by a variable  $D$ , defined as follows:

$$D = \sum \frac{\Delta \epsilon}{\epsilon^f}, \quad (17)$$

where  $\Delta \epsilon$  is the equivalent plastic strain and  $\epsilon^f$  is the equivalent strain required to fracture. Fracture occurs when  $D$  becomes 1. The general form of the fracture strain is given as follows [35]:

$$\epsilon^f = [D_1 + D_2 \exp D_3 \sigma^*][1 + D_4 \ln \epsilon^*][1 + D_5 T^*], \quad (18)$$

where  $\sigma^*$  is defined as  $\sigma_m/\bar{\sigma}$ , with  $\sigma_m$  denoting the average normal stresses and  $\bar{\sigma}$  denoting the von-Mises equivalent

stress.  $D_1$ – $D_5$  are material parameters, obtained experimentally.

**2.5. Sandwich Panel.** A sandwich structure is a structure that connects two surface layers (top and bottom) to a core in the middle [36], in order to achieve load transfer between components, which is usually used for objects that require specific standards. For example, a racing car must have the characteristics of low weight and rapid acceleration, as well as high resistance in the event of an accident [37].

Sandwich structures are also used in ships, airplanes, and various other structures. Applying the core structure helps to reduce material waste while reducing component weight. It can also increase the specific strength with the least amount of material used, increasing the structure's capacity [38]. Figure 2 shows the general structure of a sandwich panel. An air blast test is one way to understand the performance of sandwich panels under dynamic load conditions. The finite element codes allow for simulations under such dynamic conditions to be carried out without the need for destructive air blast experiments [15, 39].

**2.6. State-of-the-Art.** Research on sandwich panel structures with various configurations has been carried out before as summarized in Table 1. Pan et al. have simulated a U-shaped thin-walled steel plate with GFRP (glass fiber-reinforced plastic) honeycomb filler against a pendulum impact. The results indicated that the protective structure, designed with a thin-walled steel plate and fiber composite material, has good collision safety [40]. Wowk et al. have simulated an aluminum sandwich panel with different honeycomb core configurations and impact parameters. The experimental and numerical results demonstrated that the cellular core configuration did not significantly influence the core damage depth [41]. Luo et al. have simulated a sandwich panel with in-plane honeycombs in low-to-medium impact tests. It was found that the sandwich panels with in-plane honeycomb cores presented an elongated and stable plateau stage, with deeper and larger indentation profiles but smaller global deflections, compared to out-of-plane cores [42]. Liu et al. have simulated a U-type corrugated sandwich panel with the quasi-static compression load. The results indicated that the compression process occurs in three stages in the sandwich panel structure [27]. Khaire et al. have simulated a Honeycomb core cylindrical sandwich panel under ballistic impact. In the simulation, it was found that the transverse deflection of the hind forewings was highest, while the transverse deflection of the rear surface decreased with increasing cell wall thickness and facial skin thickness [43].

It can be concluded that research on the sandwich structure has not yet fully developed, as studies focused on the phenomenon of sandwich panel strength through a parametric study approach are still lacking. In this research, we examine the effect of geometric variations on the performance of a hull plate structure under blast loads, considering the critical role of the hull plate in military vehicles and civilian infrastructure.

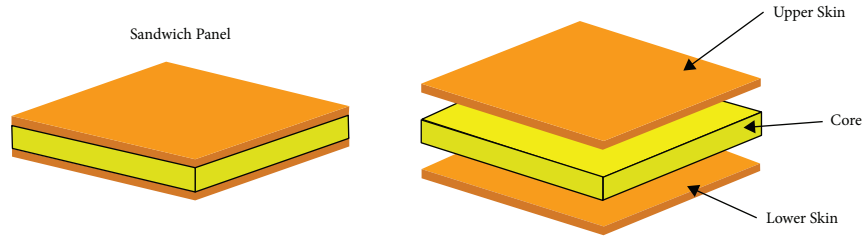


FIGURE 2: Sandwich panel construction, as used in the present study.

TABLE 1: Pioneer numerical researches on sandwich panels.

Author	Subject	Material composition	Type of loading	Conclusion
Pan et al. [40]	U-shape thin-walled steel plate with GFRP (glass fiber-reinforced plastic) honeycomb filled	Thin-walled steel plate from mild steel and fiber composite	Pendulum impact	A system horizontal impact test was carried out to examine the performance of the designed energy-absorbing structure made of a U-shaped thin-walled steel plate with GFRP (glass fiber-reinforced plastic) honeycomb filler. The results showed that the protective structure design, with thin-walled steel plate and fiber composite material, has good collision safety and can protect bridge piers well
Wowk et al. [41]	Honeycomb sandwich panel	7075T6, 2024T3 for face sheet, and 5052 H-34 for core	Low-velocity impact	Various honeycomb core configurations and impact parameters were considered experimentally using a pendulum apparatus. The damaged aluminum sandwich panel had a dent in the front, and the cell wall below the front dent was bulging. The experimental and numerical results also indicated that the configuration of the nucleus has no significant effect on the core damage depth
Luo et al. [42]	Sandwich panel with in-plane honeycombs	Aluminum	Low-to-medium impact	A comparative study of the local impact resistance of a series of hexagonal honeycombs in planes with different Poisson ratios with respect to spherical projectiles with low-to-moderate impact velocities. The mechanism of the effect of Poisson's ratio on the local impact resistance of sandwich panels was studied by considering variations in core strength and postimpact failure behavior
Liu et al. [27]	U-type corrugated Sandwich panel	Q235 steel	Quasi-static compression load	The structural deformation mechanism of U-shaped corrugated sandwich panels for ship structures under transverse quasi-static pressure loads was studied through experimental, numerical, and analytical methods. In the first and second stages, the core plates are unstable and warp from the center, after which the core plates come into contact with each other. In the third stage, the core plates are close to densification
Khaire et al. [43]	Honeycomb core cylindrical sandwich panel	Honeycomb core (AL-3003 H18) and cylindrical face sheets (AL-1100 H12)	Ballistic impact	The energy absorption and ballistic behavior of the cylindrical sandwich shells, which are comprised of honeycomb core and cylindrical face sheets, were investigated by experiments and numerical simulations. The transverse deflection of the hind forewings was highest, followed by the forelimbs and the core. The transverse deflection of the rear surface decreases with increasing cell wall thickness and facial skin thickness

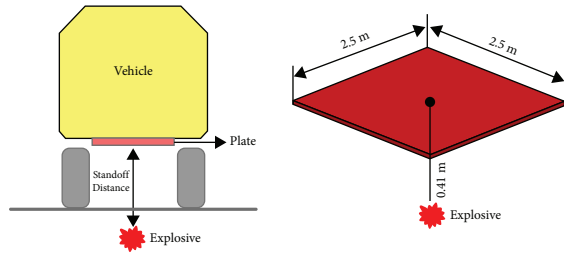


FIGURE 3: Schematics illustrating the cross-sectional view of the considered hull plate and related terminologies.

### 3. Benchmark and Mesh Strategy

**3.1. Geometrical Model.** The geometry of the simulated disk used for the benchmark analysis was  $2.5 \text{ m} \times 2.5 \text{ m} \times 0.016 \text{ m}$  (Figure 3). The geometry was adopted from the study by Markose and Rao [21], which refers to Yuen et al. [44], containing the dimensions of the Casspir armored personnel vehicle. The explosion is considered to come from a mine located  $0.41 \text{ m}$  below the surface of the central hull. Two convergence studies were performed on a  $180^\circ$  plate subjected to a  $21 \text{ kg}$  TNT load.

**3.2. Mesh Strategy.** The mesh size of a finite element model is also an essential factor affecting the numerical results, which should be small enough to allow the impacted structure to deform to its natural shape. However, very high-density meshes can significantly increase the computational resource requirements and, thus, modest cell mesh sizes are desirable. Therefore, a sensitive mesh size analysis was performed to obtain reasonable impact performance for the energy-absorbing structure [40].

The steel plate was modeled using first-order solid elements C3D8R (continuum three-dimensional 8-node reduced integration), which have minimal shear and volume locking effect. Solid elements are preferred over less time-consuming (i.e., shell) elements, as the limitations imposed by Mindlin shell theory can be avoided. The mesh size in the simulation model (Figure 4) varied, with element sizes of  $0.01 \text{ m}$  and  $0.02 \text{ m}$ .

**3.3. Benchmarking Result.** We compared the midpoint displacement values obtained in our numerical simulation with those obtained by Markose and Rao [21], as presented in Figure 5. The simulation and comparison data indicate that our result was very similar to the reference, thus validating the method we used.

### 4. Finite Element Configuration and Setting

**4.1. Blast Test Arrangement.** The explosion was assumed to come from a land mine located at a distance of  $0.41 \text{ m}$  directly below the bottom surface of the hull. We tested detonated TNT masses of  $21 \text{ kg}$ ,  $28 \text{ kg}$ , and  $35 \text{ kg}$ . In this study, the mesh used was  $0.01 \text{ m}$  and the time step was  $0.2 \text{ s}$ . The simulation was performed by determining the weight of the TNT payload, the distance of the target from the center of

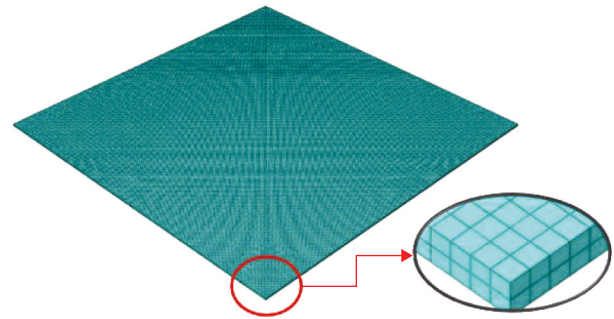


FIGURE 4: Meshed model geometry created with ABAQUS.

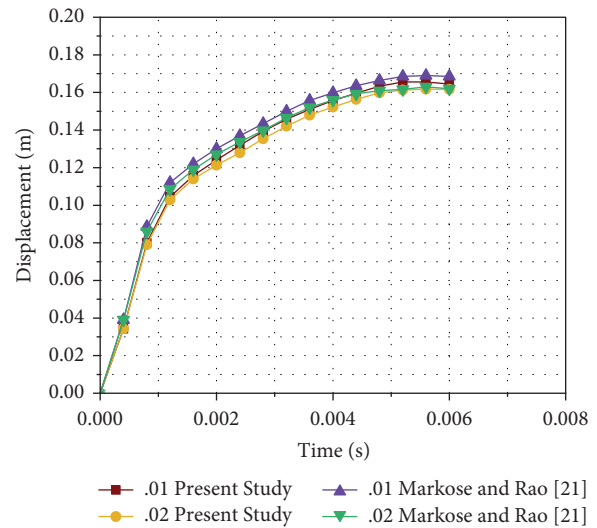


FIGURE 5: Comparison of numerical results for lower face displacement over time, with respect to the center of the plate, with those of Markose and Rao [21].

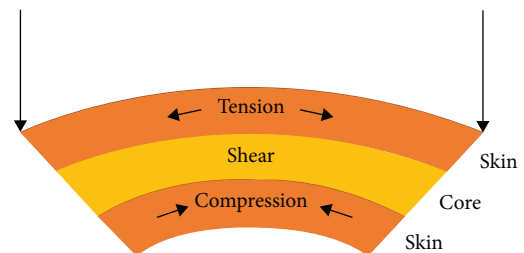


FIGURE 6: Boundary conditions for the plates.

the blast, and the geometry of the sandwich panel surface. The CONWEP explosion simulation code was then used to calculate the pressure distribution and impulse loads due to the blast load on sandwich panel surfaces with various properties.

The plates had fixed boundary conditions along the two sides parallel to the centerline, while the two remaining sides were left unconstrained (Figure 6). Symmetric boundary conditions were used, where suitable.

TABLE 2: Comparison of geometric variations.

Topology	Top view	3D view
Honeycomb		
Stiffener		
Corrugated		

4.2. *Design Variation.* We considered three variations for the core model of the sandwich panels simulated in this study (Table 2): honeycomb, stiffener, and corrugated. The thickness was used to adjust the structural weight ratio. Table 2 provides geometric descriptions of the core plates. Solid plates, as skin (top and bottom), with 0.006 m thickness were joined to cores with structural weight adjustment using eight-point continuum-3D solid elements with reduced integration (C3D8R).

4.3. *Material Properties.* Various materials and shapes can be used as energy-absorbing structures. Steel exhibits ductile and stable plastic mechanism behavior and provides a controlled and stable failure mode during the impact energy absorption process [45]. The material chosen for benchmark object simulation was mild steel, characterized by  $E = 203 \text{ GPa}$ ,  $\nu = 0.3$ , and  $\rho = 7850 \text{ kg/m}^3$ . Markose and Rao [21], referring to Iqbal et al. [46], have characterized mild steel and evaluated all material parameters in the Johnson–Cook elastoplastic model. The constants  $A$ ,  $B$ ,  $n$ ,  $C$ ,  $m$ , and  $\epsilon_0$  are material-dependent parameters, which can be determined from empirical fitting to yield stress data. The obtained parameters were verified through finite element simulations in ABAQUS.

The first material used was the same as the material used in the benchmark paper: mild steel. Mild steel, as presented

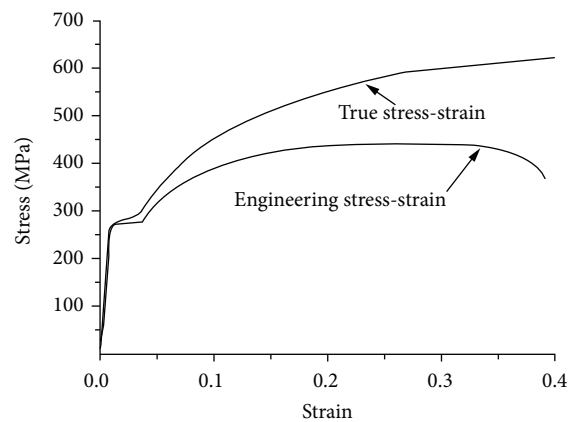


FIGURE 7: Stress-strain curves of mild steel [40].

in Figure 7, is a type of low-carbon steel. Although the range varies, depending on the source, the amount of carbon normally found in mild steel is between 0.05% and 0.25% by weight. An example of a mild steel material is ASTM A36. The properties of the used material are provided in Table 3.

The next material considered was medium carbon steel. Medium carbon steel is a material with a carbon content of around 0.3–0.8%, with microstructure that is harder and stronger. The high amount of carbon makes this steel more

TABLE 3: Material properties for mild steel [46].

Description	Notation	Numerical value
Yield stress (MPa)	$A$	304.33
Strain hardening constant (MPa)	$B$	422.007
Strain hardening coefficient (-)	$n$	0.345
Strain-rate hardening (-)	$C$	0.0156
Thermal softening constant (-)	$m$	0.87
Reference strain rate	$\epsilon_0$	$0.0001 \text{ s}^{-1}$
Melting temperature (K)	$\theta_{melt}$	1800
Transition temperature (K)	$\theta_{transition}$	293
	$D_1$	0.1152
	$D_2$	1.0116
Fracture strain constant (-)	$D_3$	-1.7684
	$D_4$	-0.05279
	$D_5$	0.5262

TABLE 4: Material properties for medium carbon steel [47].

Description	Notation	Numerical value
Yield stress (MPa)	$A$	813
Strain hardening constant (MPa)	$B$	807
Strain hardening coefficient (-)	$n$	0.73
Strain-rate hardening (-)	$C$	0.012
Thermal softening constant (-)	$m$	0.94
Reference strain rate	$\epsilon_0$	$0.0005 \text{ s}^{-1}$
Melting temperature (K)	$\theta_{melt}$	1800
Transition temperature (K)	$\theta_{transition}$	293
	$D_1$	0.0705
	$D_2$	1.732
Fracture strain constant (-)	$D_3$	-0.54
	$D_4$	-0.0123
	$D_5$	0

responsive to various heat treatment processes, improving its mechanical properties. An example of medium carbon steel material is AISI 1040. The properties of the used material are given in Table 4.

The last material used was alloy steel. Alloy steel may include any of several elements: molybdenum, manganese, nickel, chromium, vanadium, silicon, and boron. These alloying elements increase the strength, hardness, wear resistance, and toughness of the material. The amount of alloying elements can vary between 1 and 50%. Alloy steels can be classified into low-alloy steels and high-alloy steels. The boundary between low- and high-alloy steel is generally accepted as 5% of alloying element. An example of an alloy steel material is AISI 4340. The properties of the used material are provided in Table 5.

## 5. Results and Discussion

The results of 27 air blast test simulations, considering variations in core design, materials, and weight of TNT, in terms of midpoint displacement, stress contours, and internal energy, are investigated in the following sections:

**5.1. Midpoint Displacement.** The simulated core compression process is shown in Figures 8–10, which demonstrates

TABLE 5: Material properties for alloy steel [48].

Description	Notation	Numerical value
Yield stress (MPa)	$A$	792
Strain hardening constant (MPa)	$B$	510
Strain hardening coefficient (-)	$n$	0.26
Strain-rate hardening (-)	$C$	0.014
Thermal softening constant (-)	$m$	1.03
Reference strain rate	$\epsilon_0$	$1 \text{ s}^{-1}$
Melting temperature (K)	$\theta_{melt}$	1793
Transition temperature (K)	$\theta_{transition}$	298
	$D_1$	0.05
	$D_2$	3.44
Fracture strain constant (-)	$D_3$	-2.12
	$D_4$	0.002
	$D_5$	0.61

the case when a blast wave is applied to the lower skin. Considering the short time of action and the high shock frequency of the explosion, it only takes a few milliseconds from zero to maximum load. The stress-strain behavior of the structure under the action of the shock wave is positively correlated with the rate of action of the shock wave. Explosive propagation will spread to all sides after the explosion occurs. Under the unimpeded influence, the explosion wave would form a spherical wave array and spread outwards. As the blast point is relatively short (i.e., 0.41 m from the bottom layer), the short first contact with the bottom layer will increase the pressure, produce a reflected wave, and propagate over the distance. The first buckling occurs on the underside (affected side), and the bevel bends towards the inner side. Figures 11–13 show the displacement-time curves of the structure affected by the explosion. The highest deflection was located right in the center of the lower skin, closest to the blast source. However, the bevel near the top remained almost in its original state. During the movement of the lower skin, failure occurred at the bottom of the bevel, while the bevel near the top moves outward. Then, the core bent from the center to the limit, and the compression gradually reached a maximum. The dynamic global response of the core was then initiated. When the core reached maximum deflection, it started to vibrate.

The displacement value decreased farther away from the center of the plate. It can be seen that the effect of geometric variation on the collision response was very influential. It can be seen that, at time  $t=0.01 \text{ s}$ , displacement was at its highest, after which global deformation began to occur. When the face sheet reached maximum deflection, the whole plate vibrated, then returned to the static state. As can be seen from these profiles, the stiffener core model showed better maximum displacement, in comparison with the other panels.

In the contour image, it can be seen that the boundary edge also experienced movement; this was due to the boundary conditions that we used, which also affect the structure's response. However, there were some different contour results, especially at the low TNT load of 21 kg and with the medium carbon steel and alloy steel materials. For

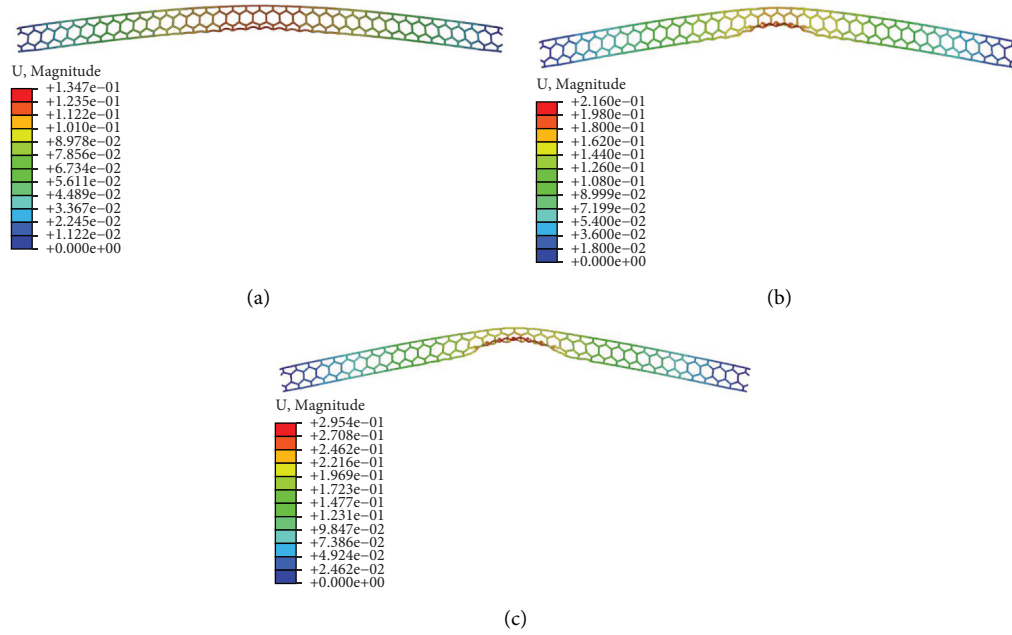


FIGURE 8: Honeycomb comparison of midpoint displacement at the time of the collision (max displacement, unit in m): (a) 21 kg, (b) 28 kg, and (c) 35 kg.

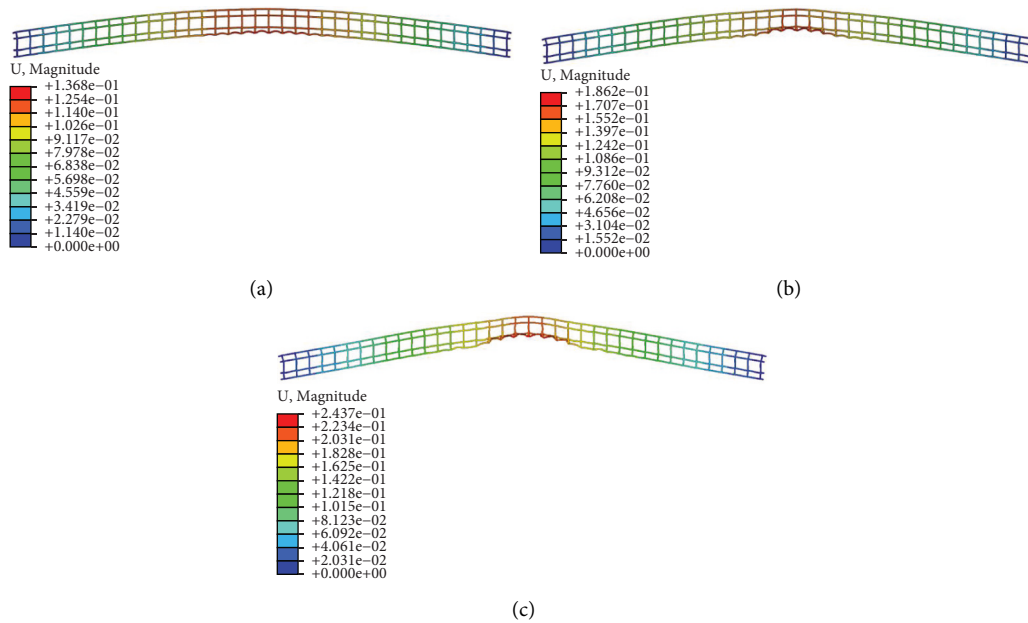


FIGURE 9: Stiffener comparison of midpoint displacement at the time of the collision (max displacement, unit in m): (a) 21 kg, (b) 28 kg, and (c) 35 kg.

the corrugated geometry model, the maximum point occurred on the front and back of the plate; this was possible because there were several significant differences in the properties of the existing material.

At a load of 21 kg, the honeycomb model obtained the best results with alloy steel material, at  $\nabla_{\max} = 0.135m$ . The stiffener model also obtained the best results with alloy steel material, with  $\nabla_{\max} = 0.136m$ . Finally, the corrugated model also obtained the best results with alloy steel material, where

$\nabla_{\max} = 0.168m$ . The worst results for all models were obtained when considering mild steel material.

At a load of 28 kg, again, the honeycomb, stiffener, and corrugated models all obtained the best results with alloy steel material ( $\nabla_{\max} = 0.216m$ ,  $0.186m$ , and  $0.207m$ , respectively). Meanwhile, the worst results for all models were obtained with the mild steel material.

Finally, for the highest TNT load (35 kg), the stiffener, honeycomb, and corrugated models all obtained the best

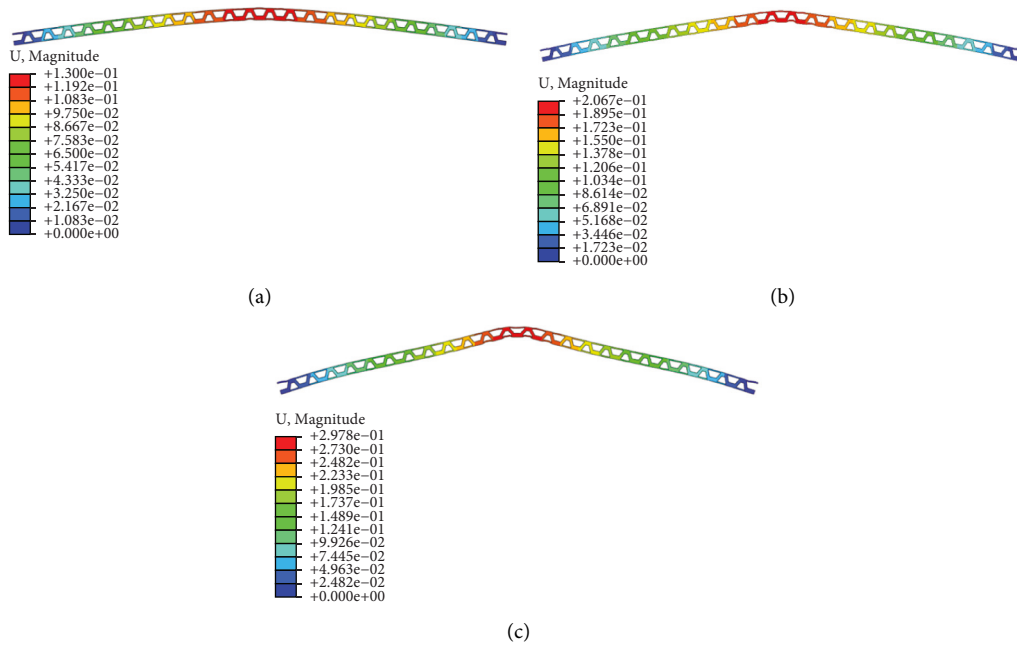


FIGURE 10: Corrugated comparison of midpoint displacement at the time of the collision (max displacement, unit in m): (a) 21 kg, (b) 28 kg, and (c) 35 kg.

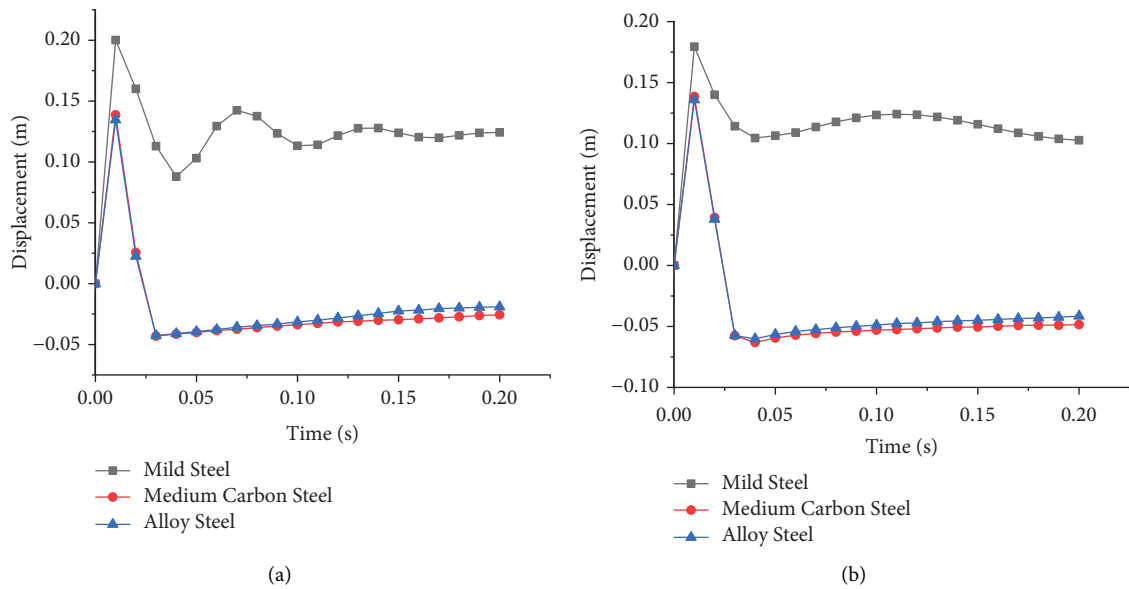
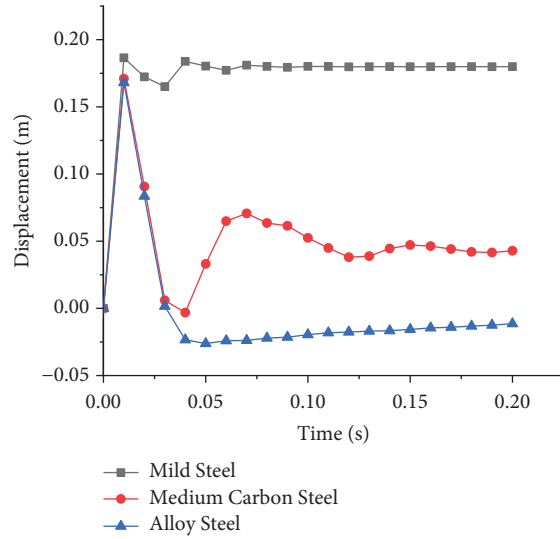
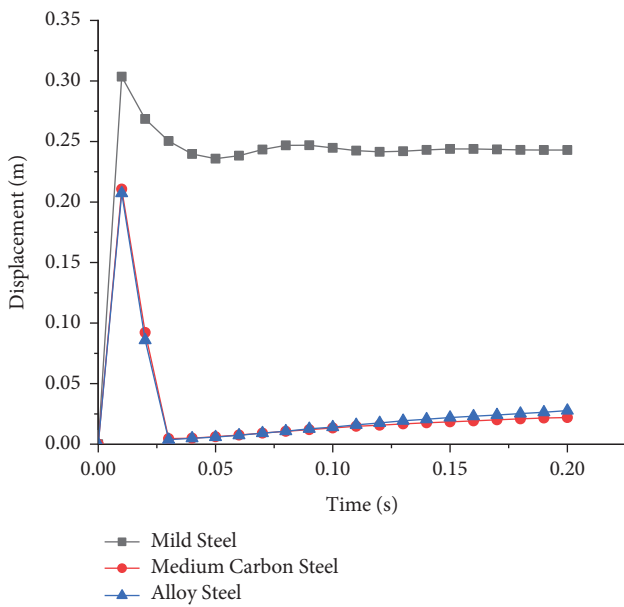


FIGURE 11: Continued.

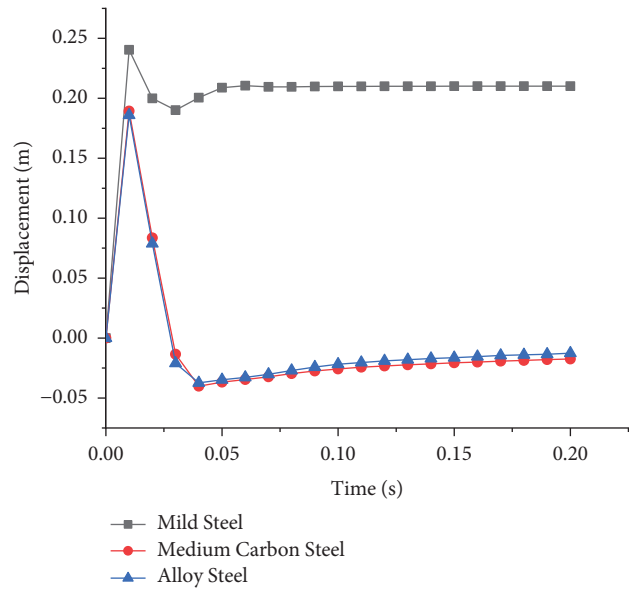


(c)

FIGURE 11: 21 kg TNT comparison with different core models (displacement-time curve): (a) honeycomb, (b) stiffener, and (c) corrugated.

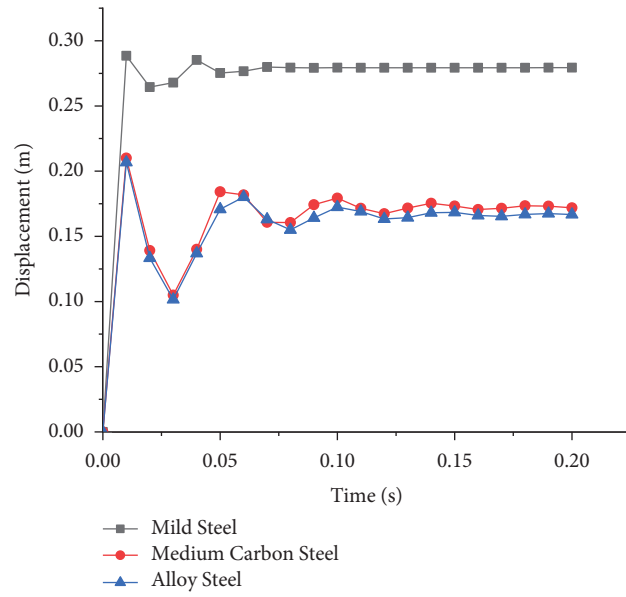


(a)



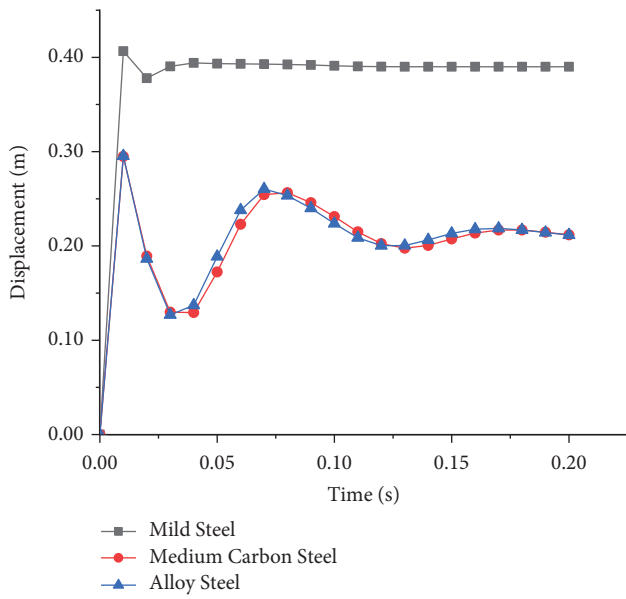
(b)

FIGURE 12: Continued.

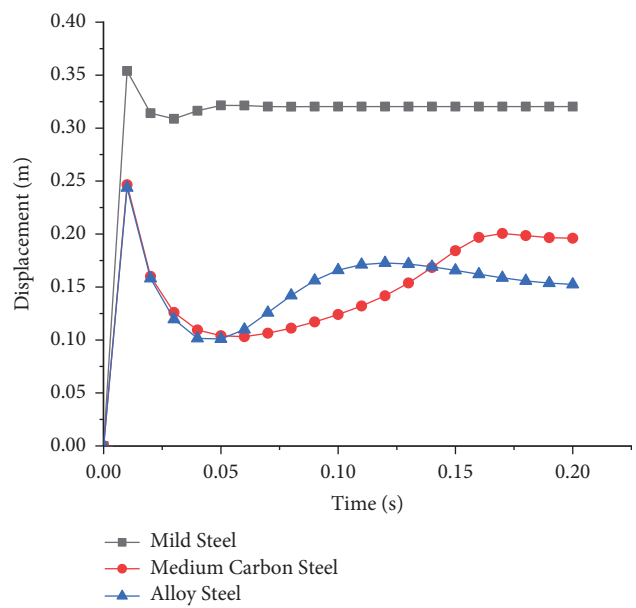


(c)

FIGURE 12: 28 kg TNT comparison for different core models (displacement-time curve): (a) honeycomb, (b) stiffener, and (c) corrugated.



(a)



(b)

FIGURE 13: Continued.

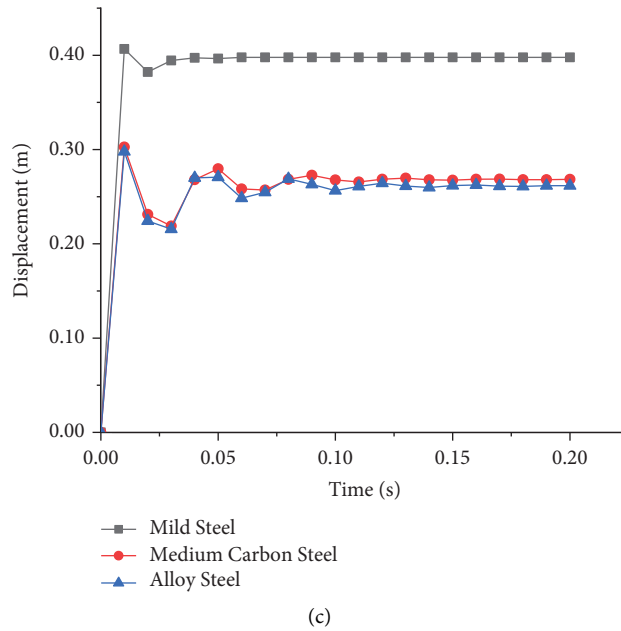


FIGURE 13: 35 kg TNT comparison for different core models (displacement-time curve): (a) honeycomb, (b) stiffener, and (c) corrugated.

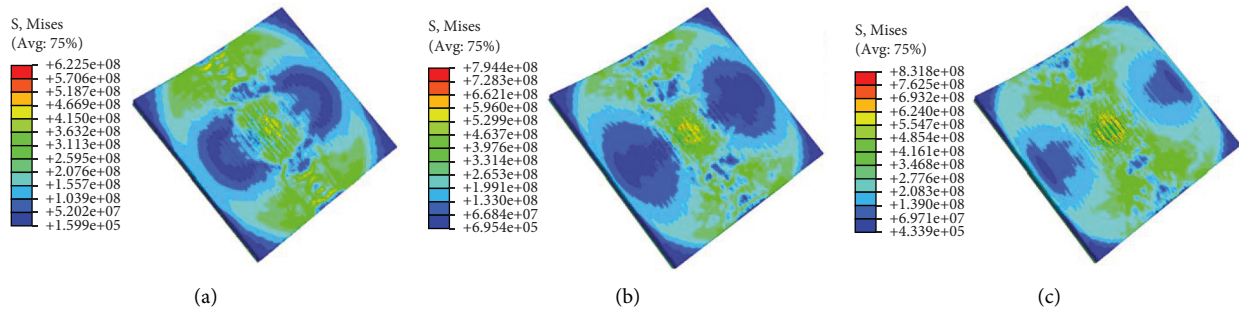


FIGURE 14: Honeycomb comparison of different load TNT at the time of the collision (von-Mises stress distribution, in Pa): (a) 21 kg, (b) 28 kg, and (c) and 35 kg.

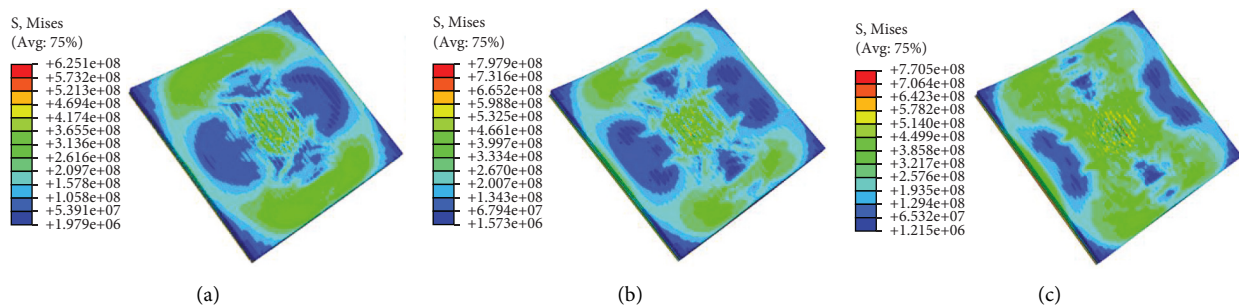


FIGURE 15: Stiffener comparison of different load TNT at the time of the collision (von-Mises stress distribution, in Pa): (a) 21 kg, (b) 28 kg, (c) and 35 kg.

results with alloy steel material ( $\nabla_{\max} = 0.244\text{m}$ ,  $0.295\text{m}$ , and  $0.298\text{m}$ , respectively). Again, the worst results were obtained with the mild steel material; in particular, for the corrugated model,  $\nabla_{\max} = 0.407\text{m}$ .

After 0.01 s, it can be seen that the plates presented a spring-back phenomenon, which occurred before the

structures produced a permanent response, as shown in terms of multiple peaks, indicating a weakening trend. In the simulation results, it can be seen that the displacements in the honeycomb, stiffener, and corrugated models with medium carbon steel and alloy steel materials at low loads were not apparent, due to significant differences in the

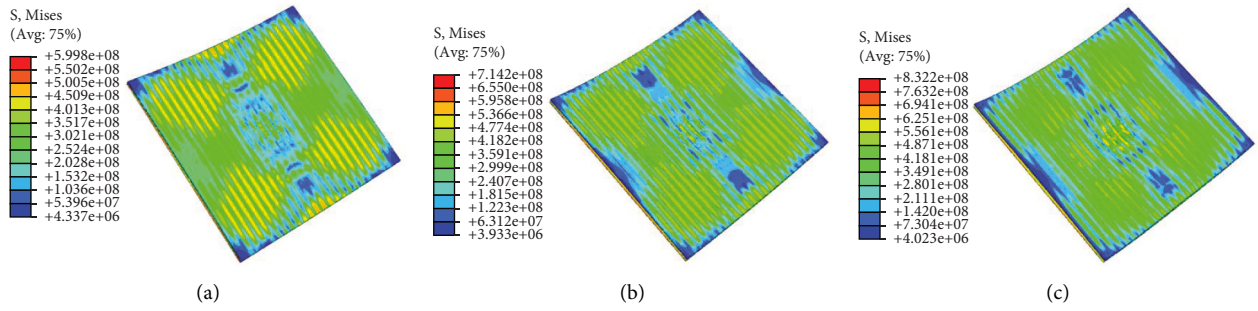


FIGURE 16: Corrugated comparison of different load TNT at the time of the collision (von-Mises stress distribution, in Pa): (a) 21 kg, (b) 28 kg, (c) and 35 kg.

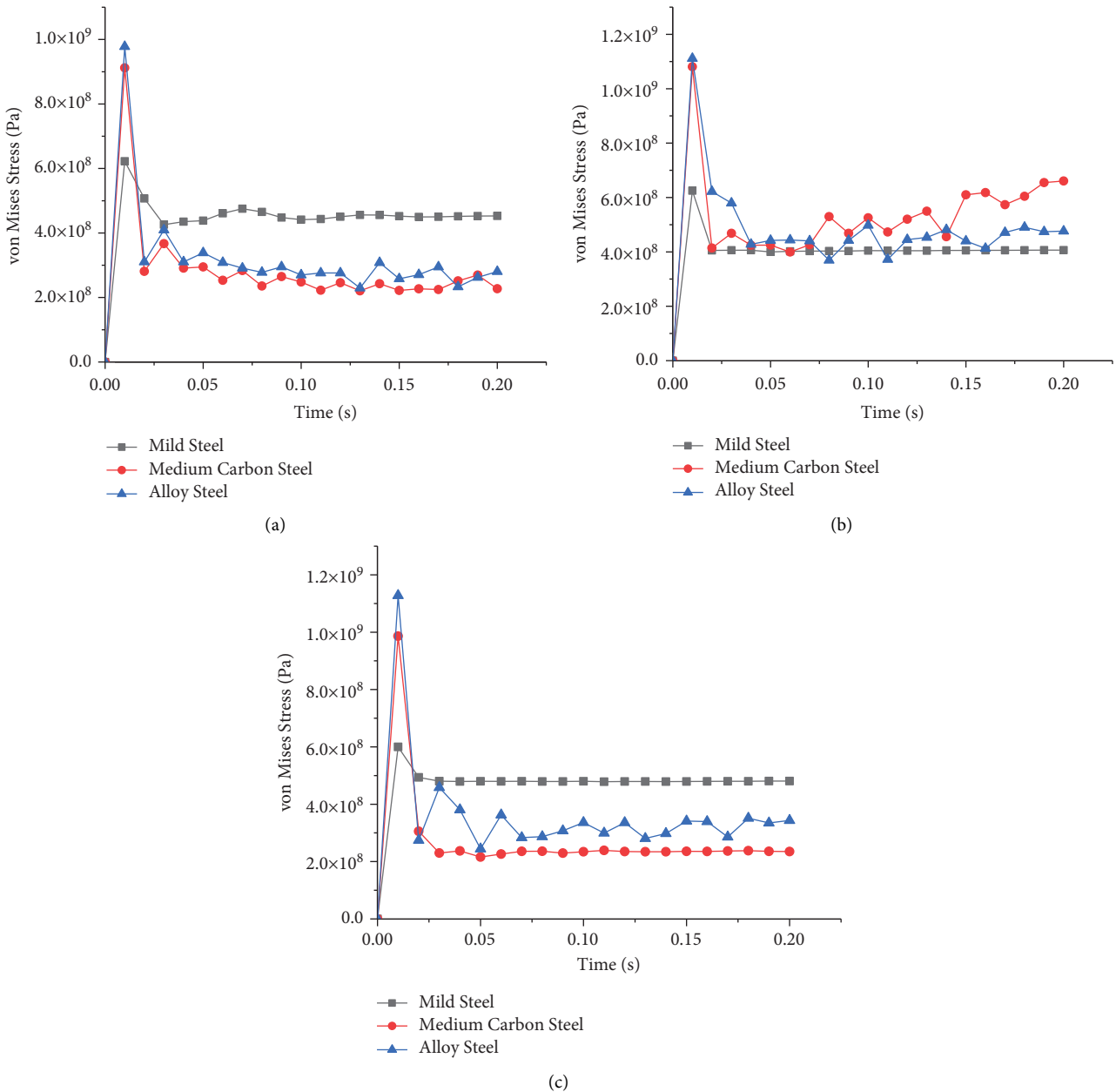


FIGURE 17: Comparison of different models and materials with 21 kg TNT load around the time of the collision (von-Mises stress distribution): (a) honeycomb, (b) stiffener, and (c) corrugated.

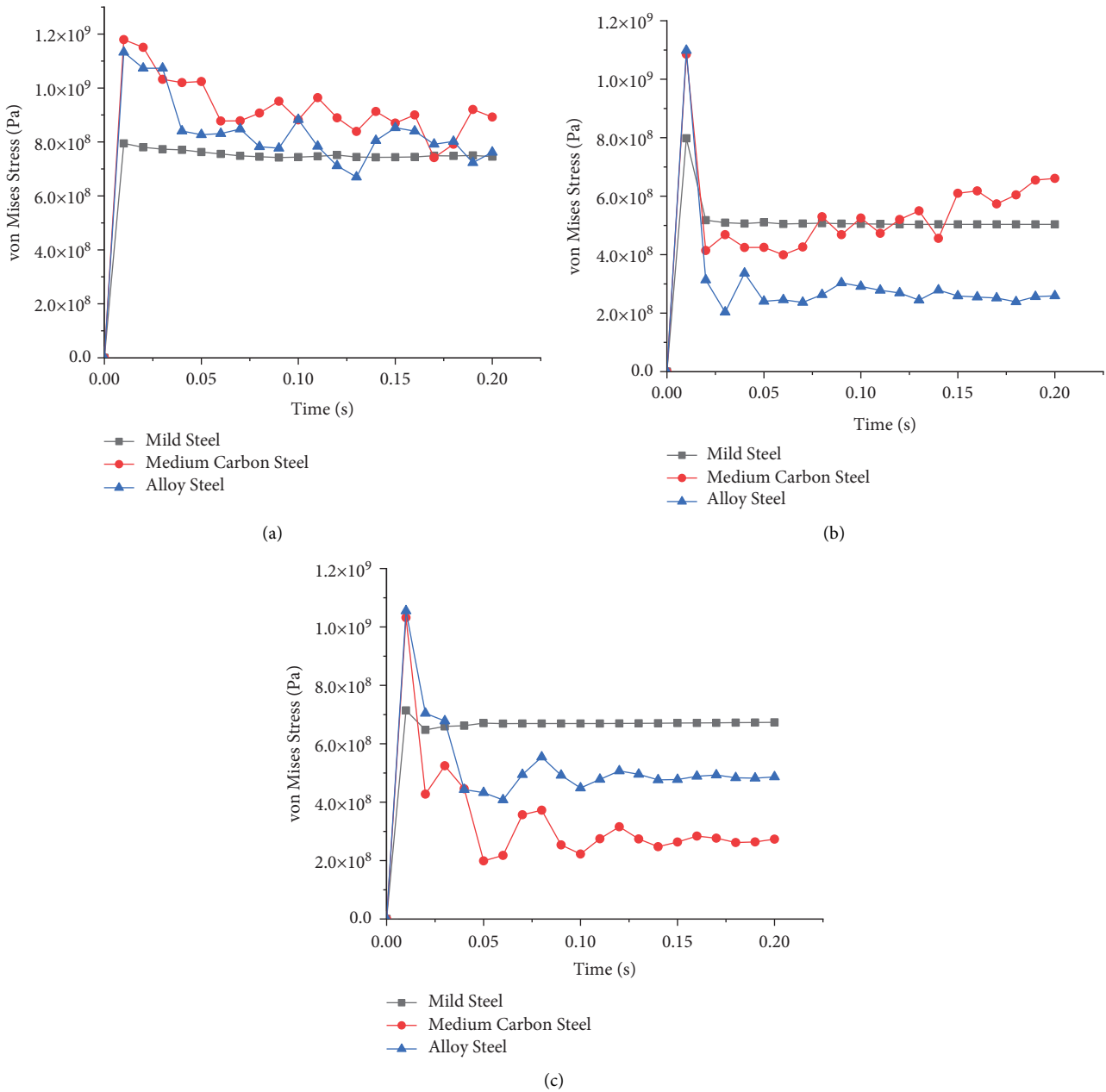


FIGURE 18: Comparison of different models and materials with 28 kg TNT load around the time of the collision (von-Mises stress distribution): (a) honeycomb, (b) stiffener, and (c) corrugated.

properties of these materials; therefore, we included yield stress in the analysis, such that the properties could be clearly determined under high-load conditions.

From the results of the simulation with the variations, it can be seen that the alloy steel material obtained the best results on average, with minimum displacement of the objects. In the second place, there was medium carbon steel, while the worst performing was mild steel. The geometric model that obtained the best average results, in terms of lower skin displacement, was stiffener. However, in terms of further observations regarding the effect of the air blast charge on the lower skin hull plate, it may be possible that the upper skin displacement presents a different order,

regarding the best geometric model, due to the shape of the core layer affecting the energy absorption. This is important to consider, as the upper skin is a plate, which is directly related to the object (vehicle).

5.2. *Stress Contour.* Snapshots of the von-Mises stress contours are shown in Figures 14–16, while the von-Mises stress distributions at the time of the collision are shown in Figures 17–19. It can be seen, from these figures, that the stress patterns of the honeycomb and stiffener panels were similar, while that of the corrugated panel differed. The contour depends on the interaction between the bottom

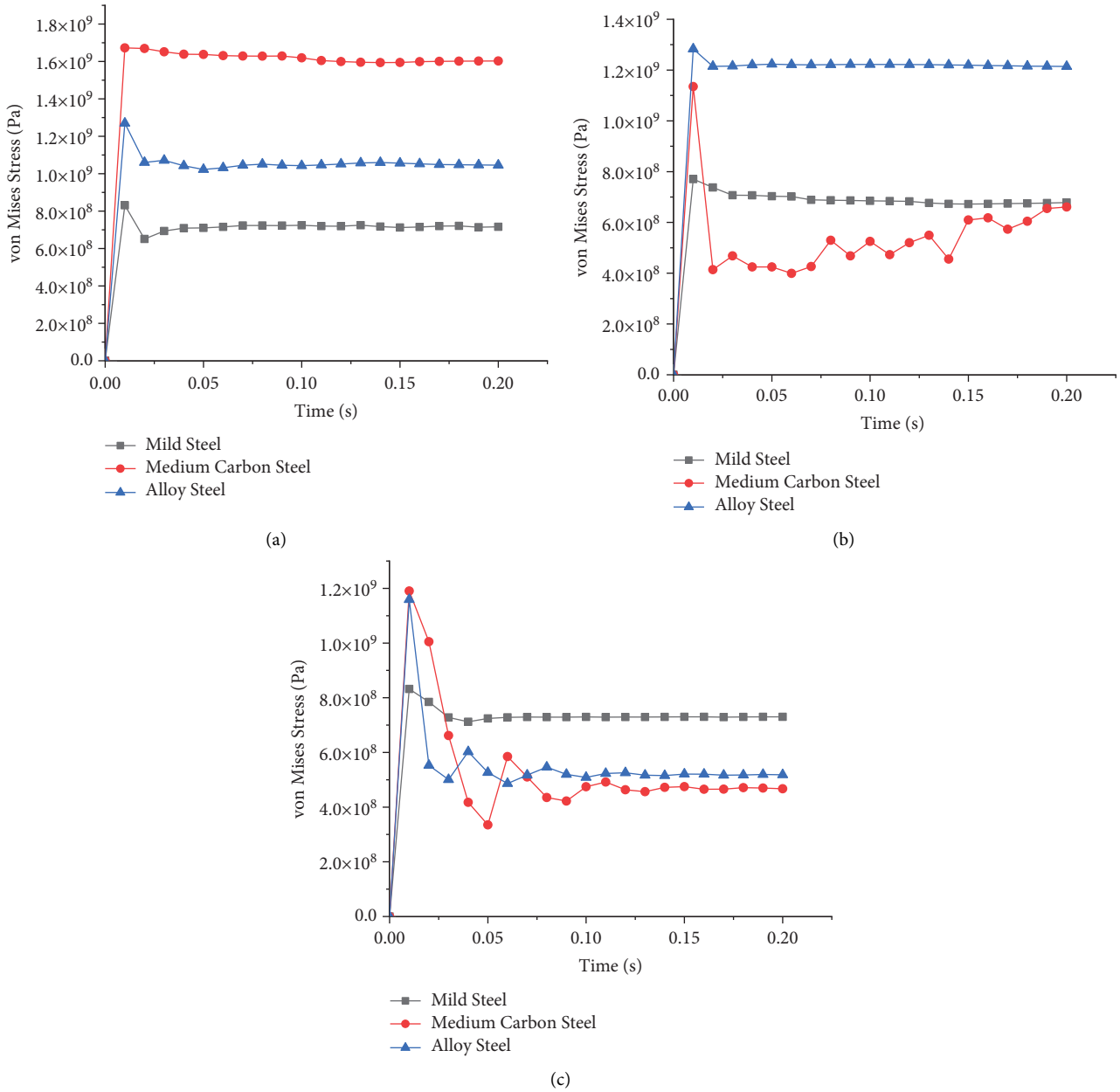


FIGURE 19: Comparison of different models and materials with 35 kg TNT load around the time of the collision (von-Mises stress distribution): (a) honeycomb, (b) stiffener, and (c) corrugated.

layer and the core, which is affected by the formation of the core's geometry using the weight ratio method. The reflected wave ring on the panel is affected by the panel boundary effect and is related to the blast wave generated at the center of the panel. In the explosion generated by the CONWEP model, the air blast is concentrated at the center of the panel and gradually spreads across the panel.

It can be seen that the stress response to the air blast in each model at the bottom of the plate was very similar. With each additional load, the area experiencing stress increased, proving that, as the load increases, the affected area also increases. This can be seen from the color of the existing structure: blue denotes lower von-Mises stress, while red indicates higher von-Mises stress. The stress contour results

also showed that the occurrence of maximum stress in the boundary area, caused by the boundary conditions used.

Stress is something that fluctuates and, so, its distribution at a certain point in time cannot be representative of the entire process. Therefore, we also provide graphs of the time history of the von-Mises stress values:

At a load of 21 kg, the honeycomb, stiffener, and corrugated models all obtained the highest von-Mises stress value with the alloy steel material ( $\sigma = 9.79 \times 10^8$  Pa,  $1.11 \times 10^9$  Pa, and  $1.13 \times 10^9$  Pa, respectively). Meanwhile, the lowest results for all models were obtained with the mild steel material.

At a load of 28 kg, the honeycomb model obtained the highest von-Mises stress with the medium carbon steel

TABLE 6: Details of used abbreviations.

Abbreviation	Description
ALLAE	Artificial strain energy is associated with constraints that are used to remove singular modes. Also, it is related to constraints that are used to force the drill rotation to follow the in-plane rotation of the shell elements
ALLIE	Total strain energy (ALLIE = ALLSE + ALLPD + ALLCD + ALLAE + ALLDMD + ALLDC + ALLFC)
ALLKE	Kinetic energy
ALLPD	Energy dissipated by rate-independent and rate-dependent plastic deformation
ALLSE	Recoverable strain energy

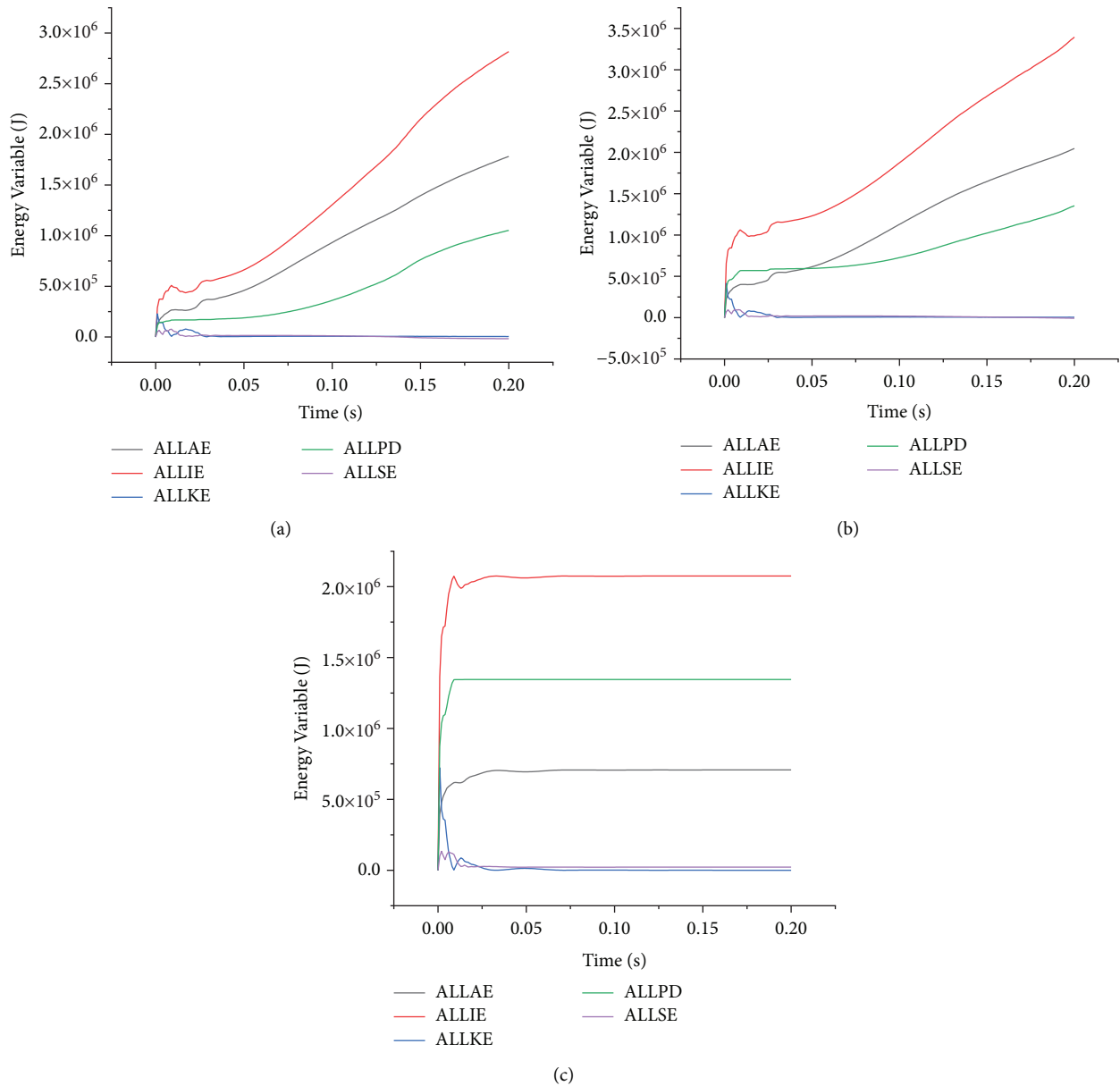


FIGURE 20: Comparison of the honeycomb model with different TNT loads, in terms of internal energy and kinetic energy: (a) 21 kg, (b) 28 kg, and (c) 35 kg.

material, at  $\sigma = 1.18 \times 10^9$  Pa. Meanwhile, in the stiffener and corrugated models, the maximum value was obtained with the alloy steel material ( $\sigma = 1.09 \times 10^9$  Pa and  $1.05 \times 10^9$  Pa, respectively). Again, the lowest results for all models were obtained with the mild steel material.

At a load of 35 kg, the honeycomb and corrugated models obtained the highest von-Mises stress with medium carbon steel material ( $\sigma = 1.67 \times 10^9$  Pa and  $1.19 \times 10^9$ , respectively). Meanwhile, for the stiffener model, the maximum value was obtained with the alloy steel material

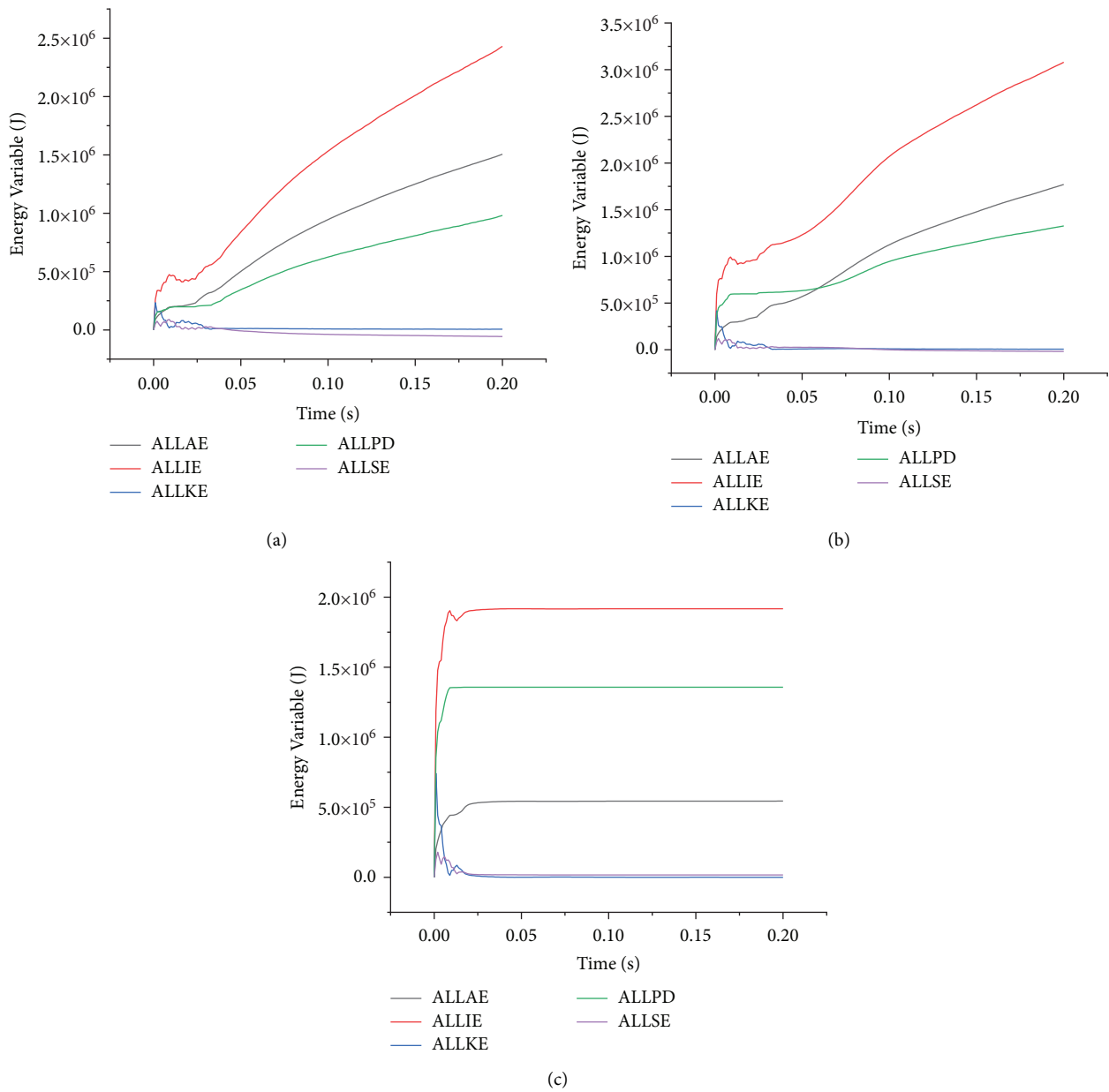


FIGURE 21: Comparison of the stiffener model with different TNT loads, in terms of internal energy and kinetic energy: (a) 21 kg, (b) 28 kg, and (c) 35 kg.

( $\sigma = 1.28 \times 10^9$  Pa). Once more, the lowest results for all models were obtained with the mild steel material.

The simulation results indicated that the von-Mises stresses for honeycomb, stiffener, and corrugated models with mild steel, medium carbon steel, and alloy steel materials well defined the stress obtained with each geometric model and material used. The data show that the stress was at its maximum after the TNT had detonated and the shock wave hit the hull plate. The results demonstrated that mild steel has less fluctuations in stress (i.e., tending to be flat), when compared to the other materials. This was due to the fact that there are several significant differences in the properties of the considered materials, as previously mentioned.

Stress variations can vary, depending on how many step times are considered in the sample. The graphs above considered a time step of 0.01 s, in order to measure the maximum von-Mises stress. It can be seen that all materials and models had almost the same trend in their stress history. After reaching a peak, the stress immediately decreased, with vibration occurring at the following step time. The stress behavior of the objects in this simulation can be determined through analysis of the necessary conditions, including the magnitude of the blast load, the thickness of the hull plate, the modulus of elasticity, and the Poisson ratio.

5.3. *Structure Internal and Kinetic Energy.* Energy output is often an important part of ABAQUS/Explicit analysis.

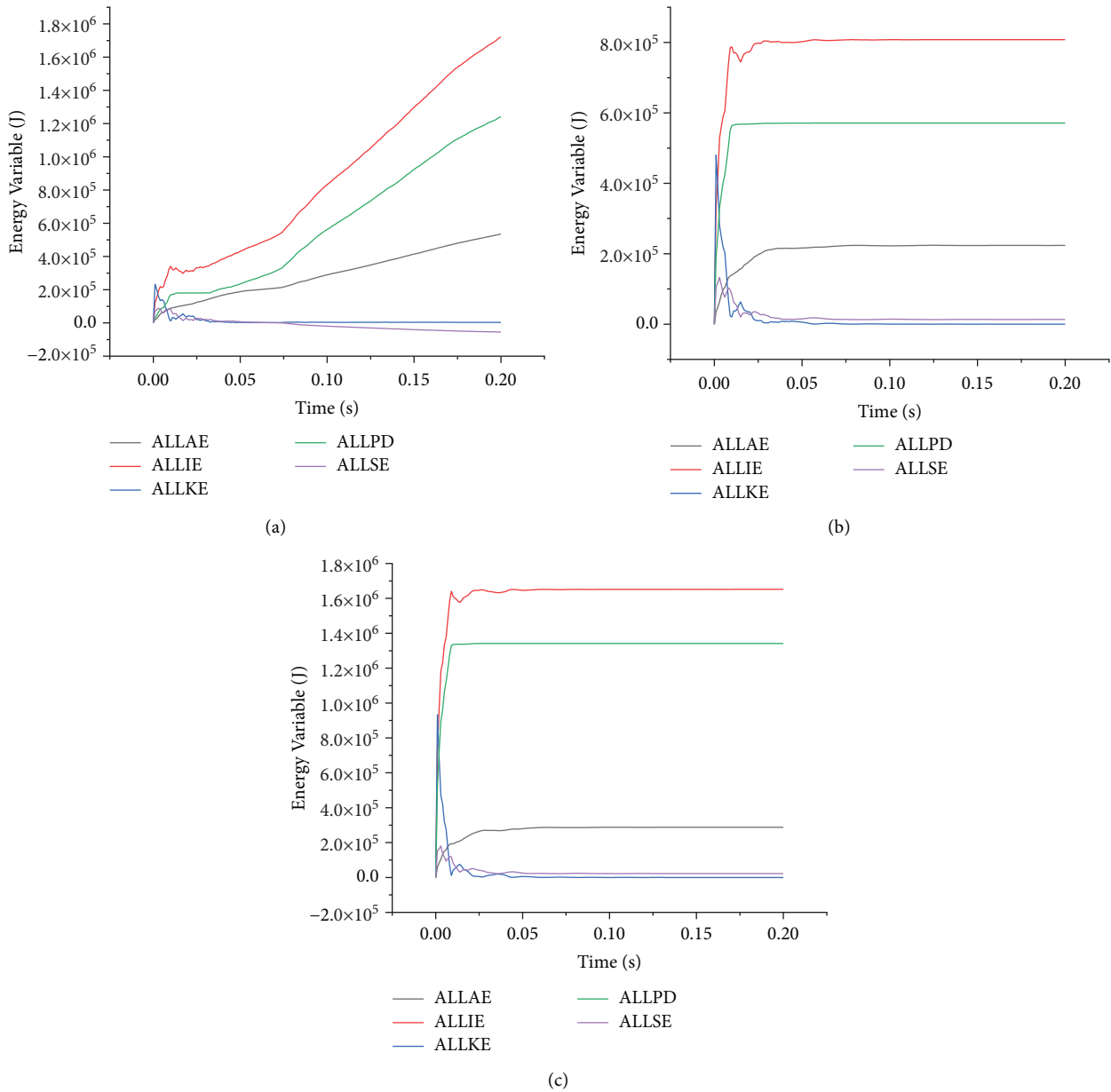


FIGURE 22: Comparison of the corrugated model with different TNT loads, in terms of internal energy and kinetic energy: (a) 21 kg, (b) 28 kg, and (c) 35 kg.

Comparisons between the various components of energy can be used to help evaluate whether an analysis produces an appropriate response. The components and their abbreviation are summarized in Table 6.

Figures 20–22 show that, after the blast wave loading had completed, the plate began to vibrate, where the kinetic energy of ALLKE increased and the strain energy of ALLSE began to decrease. The strain energy was greatest when the plate had deformed the most, and least when the plate was vibrating at other times. The plastic strain energy of ALLPD reached a steady state and increased with time. The kinetic energy diagram indicates that a second expansion of the plastic strain energy occurred as the plate recovered from its maximum deformation. Therefore, plastic deformation after blast wave loading was observed. In ABAQUS, the

deformation of an hourglass-shaped element is controlled by the quantity ALLAE (virtual strain energy). The results demonstrate that the plastic deformation corresponds to the deformation of the structure when the internal energy dissipates, and the total internal energy itself is much higher than the sum of the elastic strain energies. Therefore, it can be concluded that the virtual strain energy in this analysis is a type of quantum energy, including dissipative energy and elastic strain energy. ALLIE is the total internal strain energy (ALLSE + ALLPD + ALLAE), including all internal energies [49].

It can be seen, from the simulation results, that the internal and kinetic energy presented a similar trend, as they should. However, in some simulations (i.e., medium carbon steel and alloy steel materials in honeycomb, stiffener, and

corrugated models at low loads of 21 and 28 kg), different trends were observed up to 0.2 s, as ALLAE, ALLIE, and ALLPD continued to increase. This was due to the significant differences in the properties of these materials, including the yield stress. The trend was expected to be clearly seen at the highest TNT load; however, at the highest TNT load, all geometric models presented the same graphic pattern. In the perfectly formed graph, the history patterns of medium carbon steel and alloy steel, to be precise; it can be seen that ALLIE has a steeper turning point, compared to that with mild steel.

From the figures, it can be seen that the honeycomb model had the highest maximum average values of ALLAE and ALLIE, the stiffener model had the highest maximum average values of ALLKE and ALLPD, and the corrugated model had the highest maximum average value on ALLSE. This can be more clearly seen at the highest load of TNT (35 kg), where ALLAE and ALLIE for the honeycomb model with alloy steel material are 707,672 J and 2,075,160 J, respectively; ALLKE and ALLPD in the stiffener model with the same material were 742,631 J and 1,357,130 J, respectively; ALLSE of the corrugated model with the same material was 180,238 J.

## 6. Conclusions

In this study, a numerical investigation of the dynamic response and internal kinetic energy of sandwich panels with various structural and material combinations was carried out. In particular, simulations were carried out using three different variations of the core geometry (honeycomb, stiffener, and corrugated), through equations using structural weights. We found that using a sandwich panel structure with stiffener or honeycomb core geometry can provide an appropriate means to increase the structural resistance against explosions, serving as an exciting innovation or a substitute for the conventional (i.e., corrugated) form. Their structural performance was found to be more effective, in terms of minimizing the damage caused by explosion loads. Simulation was carried out with several variations, including the different geometric core models with mild steel, medium carbon steel, and alloy steel materials. The test was conducted using the CONWEP method in the ABAQUS software, considering free air blast under a TNT load of 21 kg, 28 kg, or 35 kg. In this simulation, we assessed the impact of the free air blast on the hull plate, in terms of displacement, von-Mises stress, and internal kinetic energy.

The simulation results indicated each structural variation's ability to withstand the free air blast load. It can be seen from the displacement results that sandwich plates with a core stiffener form were more effective in resisting the various blast loads. We also obtained the best displacement results when using the alloy steel material. It was concluded that a stiffener geometric model with an alloy steel material provides the best combination of shape and material.

The stiffener model obtained the best results regarding the maximum displacement of the lower skin; however, for the upper skin, it was found that the honeycomb had the best

displacement results, demonstrating that the honeycomb core model provided the best energy absorption. The simulation results showed that the von-Mises stress of honeycomb, stiffener, and corrugated models with mild steel, medium carbon steel, and alloy steel materials well defined the stress for each geometric model and material used. The resultant graphs showed that all of the combinations experienced a point of maximum stress right after the explosion load, while experiencing vibrations afterward.

For optimal results, the core structure must provide the necessary supporting stiffness to spread the impact forces at the contact points throughout the structure. More complex core, material, and corner models may be considered in further research, in order to enhance the model strength while developing advanced lightweight designs.

## Data Availability

The data used to support the findings of this study are included within the article.

## Conflicts of Interest

The authors declare that they have no conflicts of interest.

## Acknowledgments

This research was funded by the Universitas Sebelas Maret under funding scheme Kolaborasi Internasional (KI-UNS) with contract/grant no. 254/UN27.22/PT.01.03/2022. The grant is gratefully acknowledged by the authors.

## References

- [1] S. Fordham, *High Explosives and Propellants*, Elsevier, Amsterdam, 2013.
- [2] F. Beshara, "Modelling of blast loading on aboveground structures—I. General phenomenology and external blast," *Computers & Structures*, vol. 51, no. 5, pp. 585–596, 1994.
- [3] A. M. Remennikov, "A review of methods for predicting bomb blast effects on buildings," *Journal of Battlefield Technology*, vol. 6, p. 5, 2003.
- [4] M. A. Husni Mubarak, T. Muttaqie, A. R. Prabowo, J. M. Sohn, E. Surojo, and F. Imaduddin, "Effects of geometrical variations on the performance of hull plate structures under blast load: a study using nonlinear fea," *Procedia Structural Integrity*, vol. 41, pp. 282–289, 2022.
- [5] A. R. Prabowo and D. M. Bae, "Environmental risk of maritime territory subjected to accidental phenomena: correlation of oil spill and ship grounding in the Exxon Valdez's case," *Results in Engineering*, vol. 4, Article ID 100035, 2019.
- [6] A. R. Prabowo, Q. Thang Do, B. Cao, and D. M. Bae, "Land and marine-based structures subjected to explosion loading: a review on critical transportation and infrastructure," *Procedia Structural Integrity*, vol. 27, pp. 77–84, 2020.
- [7] A. Fajri, A. R. Prabowo, and N. Muhyat, "Assessment of ship structure under fatigue loading: FE benchmarking and extended performance analysis," *Curved and Layered Structures*, vol. 9, no. 1, pp. 163–186, 2022.
- [8] A. R. Prabowo, T. Tuswan, and R. Ridwan, "Advanced development of sensors' roles in maritime based industry and

- research: from field monitoring to high risk phenomenon measurement,” *Applied Sciences*, vol. 11, no. 9, p. 3954, 2021.
- [9] D. T. A. Ansori, A. R. Prabowo, T. Muttaqie et al., “Investigation of honeycomb sandwich panel structure using aluminum alloy (AL6XN) material under blast loading,” *Civil Engineering Journal*, vol. 8, no. 5, pp. 1046–1068, 2022.
- [10] F. H. A. Alwan, A. R. Prabowo, T. Muttaqie, N. Muhayat, R. Ridwan, and F. B. Laksono, “Assessment of ballistic impact damage on aluminum and magnesium alloys against high velocity bullets by dynamic FE simulations,” *Journal of the Mechanical Behavior of Materials*, vol. 31, no. 1, pp. 595–616, 2022.
- [11] A. R. Prabowo, R. Ridwan, and T. Muttaqie, “On the resistance to buckling loads of idealized hull structures: FE analysis on designed-stiffened plates,” *Design*, vol. 6, no. 3, p. 46, 2022.
- [12] A. R. Prabowo, T. Tuswan, A. Nurcholis, and A. A. Pratama, “Structural resistance of simplified side hull models accounting for stiffener design and loading type,” *Mathematical Problems in Engineering*, vol. 2021, pp. 1–19, 2021.
- [13] D. F. Smaradhana, A. R. Prabowo, and A. N. F. Ganda, “Exploring the potential of graphene materials in marine and shipping industries – a technical review for prospective application on ship operation and material-structure aspects,” *Journal of Ocean Engineering and Science*, vol. 6, no. 3, pp. 299–316, 2021.
- [14] Landmine Monitor Report, “Landmine Casualties “exceptionally High”, Syria and Afghanistan Worst-Hit,” 2021, <https://news.un.org/en/story/2021/11/1105432>.
- [15] G. S. Langdon, S. K. Yuen, and G. N. Nurick, “Experimental and numerical studies on the response of quadrangular stiffened plates. Part II: localised blast loading,” *International Journal of Impact Engineering*, vol. 31, no. 1, pp. 85–111, 2005.
- [16] A. Chen, L. A. Louca, and A. Y. Elghazouli, “Blast assessment of steel switch boxes under detonation loading scenarios,” *International Journal of Impact Engineering*, vol. 78, pp. 51–63, 2015.
- [17] P. L. Sachdev, *Shock Waves and Explosions, Monographs and Surveys in Pure and Applied Mathematics*, Chapman & Hall, London, 2004.
- [18] J. W. Hutchinson and Z. Xue, “Metal sandwich plates optimized for pressure impulses,” *International Journal of Mechanical Sciences*, vol. 47, no. 4-5, pp. 545–569, 2005.
- [19] K. P. Dharmasena, H. N. G. Wadley, Z. Xue, and J. W. Hutchinson, “Mechanical response of metallic honeycomb sandwich panel structures to high-intensity dynamic loading,” *International Journal of Impact Engineering*, vol. 35, no. 9, pp. 1063–1074, 2008.
- [20] H. Zhu and S. K. Khanna, “Dynamic response of a novel laminated glass panel using a transparent glass fiber-reinforced composite interlayer under blast loading,” *International Journal of Impact Engineering*, vol. 89, pp. 14–24, 2016.
- [21] A. Markose and C. L. Rao, “Mechanical response of V shaped plates under blast loading,” *Thin-Walled Structures*, vol. 115, pp. 12–20, 2017.
- [22] M. D. Goel and V. A. Matsagar, “Blast-resistant design of structures,” *Practice Periodical on Structural Design and Construction*, vol. 19, no. 2, Article ID 04014007, 2014.
- [23] “Joint department of the army, the navy and the air force,” *TM 5-1330(1990), Structures to Resist the Effects of Accidental Explosions*, Department of Defence Explosives Safety Board, Alexandria, Virginia, 1990.
- [24] Bureau of Indian Standards (Bis)Criteria for Blast Resistant Design of Structures for Explosions above Ground, New Delhi, India, 1968.
- [25] Bureau of Indian Standards (Bis)Criteria for Safety and Design of Structures Subject to Underground Blasts, New Delhi, India, 1973.
- [26] U.S, *TM 5-855-1(1986), Design & Analysis of Hardened Structures to Conventional Weapons Effects*, Department of the Army, Washington DC, 1986.
- [27] K. Liu, S. Zong, Y. Li, Z. Wang, Z. Hu, and Z. Wang, “Structural response of the U-type corrugated core sandwich panel used in ship structures under the lateral quasi-static compression load,” *Marine Structures*, vol. 84, Article ID 103198, 2022.
- [28] F. Zhu and G. Lu, “A review of blast and impact of metallic and sandwich structures,” *Electronic Journal of Structural Engineering*, no. 1, pp. 92–101, 2007.
- [29] R. Courant, K. Friedrichs, and H. Lewy, “Über die partiellen differenzgleichungen der mathematischen physik,” *Mathematische Annalen*, vol. 100, no. 1, pp. 32–74, 1928.
- [30] P. Longère, A. G. Geffroy-Grèze, B. Leblé, and A. Dragon, “Ship structure steel plate failure under near-field air-blast loading: numerical simulations vs. experiment,” *International Journal of Impact Engineering*, vol. 62, pp. 88–98, 2013.
- [31] J. Lee, T. E. Lacy, and C. U. Pittman, “Lightning mechanical damage prediction in carbon/epoxy laminates using equivalent air blast overpressure,” *Composites Part B: Engineering*, vol. 212, Article ID 108649, 2021.
- [32] V. Karlos, G. Solomos, and B. Viacoz, *Calculation of Blast Loads for Application to Structural Components*, Publications Office, 2013.
- [33] D. W. Hyde, *CONWEP: Conventional Weapons Effects Program*, MSVicksburg, Vicksburg, 1991.
- [34] S. Yadav, S. Singhal, Y. Jasra, and R. K. Saxena, “Determination of Johnson-Cook material model for weldment of mild steel,” *Materials Today Proceedings*, vol. 28, pp. 1801–1808, 2020.
- [35] G. R. Johnson and W. H. Cook, “Fracture characteristics of three metals subjected to various strains, strain rates, temperatures and pressures,” *Engineering Fracture Mechanics*, vol. 21, no. 1, pp. 31–48, 1985.
- [36] A. Røsdal, *Analysis and optimization of sandwich panels-Master’s Thesis*, 2017.
- [37] DIABgroup, *Guide to Core and Sandwich*, pp. 1–48, DIA-Bgroup, Laholm, Sweden, 2012.
- [38] P. K. Chawa and S. K. Mukkamala, *Design and analysis of shipping container made of honeycomb sandwich panels*, vol. 7, Department of Mechanical Engineering Blekinge Institute of Technology, Karlskrona, Sweden, 2018, Master’s Degree Thesis.
- [39] S. Chung Kim Yuen and G. N. Nurick, “Experimental and numerical studies on the response of quadrangular stiffened plates. Part I: subjected to uniform blast load,” *International Journal of Impact Engineering*, vol. 31, no. 1, pp. 55–83, 2005.
- [40] J. Pan, H. Fang, M. C. Xu, and Y. F. Wu, “Study on the performance of energy absorption structure of bridge piers against vehicle collision,” *Thin-Walled Structures*, vol. 130, pp. 85–100, 2018.
- [41] D. Wolk, T. Reyno, R. Yeung, and C. Marsden, “An experimental and numerical investigation of core damage size in honeycomb sandwich panels subject to low-velocity impact,” *Composite Structures*, vol. 254, Article ID 112739, 2020.
- [42] Y. Luo, K. Yuan, L. Shen, and J. Liu, “Sandwich panel with in-plane honeycombs in different Poisson’s ratio under low to medium impact loads,” *Reviews on Advanced Materials Science*, vol. 60, no. 1, pp. 145–157, 2021.

- [43] N. Khaire, G. Tiwari, S. Rathod, M. A. Iqbal, and A. Topa, "Perforation and energy dissipation behaviour of honeycomb core cylindrical sandwich shell subjected to conical shape projectile at high velocity impact," *Thin-Walled Structures*, vol. 171, Article ID 108724, 2022.
- [44] S. Chung Kim Yuen, G. S. Langdon, G. N. Nurick, E. G. Pickering, and V. H. Balden, "Response of V-shape plates to localised blast load: experiments and numerical simulation," *International Journal of Impact Engineering*, vol. 46, pp. 97–109, 2012.
- [45] T. Wierzbicki and W. Abramowicz, *on the Crushing Mechanics of Thin-Walled Structures*, Vol. 83, American Society of Mechanical Engineers (ASME), , New York, 1983.
- [46] M. A. Iqbal, K. Senthil, P. Bhargava, and N. K. Gupta, "The characterization and ballistic evaluation of mild steel," *International Journal of Impact Engineering*, vol. 78, pp. 98–113, 2015.
- [47] H. Purwanto, M. Dzulfikar, M. Tauviqirrahman, R. Subagyo, and Kiryanto, "Ballistic limit simulation on commercial medium carbon steel plate with surface hardening using an induction heating," *IOP Conference Series: Materials Science and Engineering*, vol. 1034, no. 1, Article ID 012148, 2021.
- [48] T. Mabrouki and J. F. Rigal, "A contribution to a qualitative understanding of thermo-mechanical effects during chip formation in hard turning," *Journal of Materials Processing Technology*, vol. 176, no. 1-3, pp. 214–221, 2006.
- [49] H. Reissmann and P. S. Pawlik, *Elasticity, Theory and Applications*, Krieger Publishing Company, Malabar, Florida, 1991.